Nano Research

ISSN 1998-0124 CN 11-5974/O4
https://doi.org/10.26599/NR.2026.94909067

Research Article

Cross-linking engineering of starch molecular topology tailoring hard carbon microstructure and sodium storage kinetics

Yongling Men[1], Qingsang He[1], Jiyue Hou[1], Yiyong Zhang[1], Ziyi Zhu[1](✉), Yingjie Zhang[1,2](✉), Xue Li[1](✉)

[1] National and Local Joint Engineering Research Center of Lithium-ion Batteries and Materials Preparation Technology, Key Laboratory of Advanced Battery Materials of Yunnan Province, School of Metallurgical and Energy Engineering, Kunming University of Science and Technology, Kunming 650500, China

[2] Southwest United Graduate School, Kunming 650092, China

Nano Res., **Just Accepted Manuscript** • https://doi.org/10.26599/NR.2026.94909067

https://www.sciopen.com/journal/1998-0124 on Jul. 31, 2026

Just Accepted

Research Article

Cross-linking engineering of starch molecular topology tailoring hard carbon microstructure and sodium storage kinetics

Yongling Men[1], Qingsang He[1], Jiyue Hou[1], Yiyong Zhang[1], Ziyi Zhu[1*], Yingjie Zhang[1,2*], and Xue Li[1*]

[1]National and Local Joint Engineering Research Center of Lithium-ion Batteries and Materials Preparation Technology, Key Laboratory of Advanced Battery Materials of Yunnan Province, School of Metallurgical and Energy Engineering, Kunming University of Science and Technology, Kunming 650500, China

[2]Southwest United Graduate School, Kunming 650092, China

Received: 11 June 2026; **Revised:** 23 July 2026; **Accepted:** 31 July 2026

Address correspondence to Ziyi Zhu, zyzhu23@kust.edu.cn; Yingjie Zhang, zyjkmust@126.con; Xue Li, Lixue@kust.edu.cn

Cite this article: *Nano Research*, 2026, 19, 94909067 https://doi.org/10.26599/NR.2026.94909067

Abstract

Owing to the abundance and low cost of their precursors, along with their superior sodium storage capability, biomass-derived hard carbons hold great promise as anodes for sodium-ion batteries. However, how precursor molecular structure governs hard carbon properties remains unclear. Herein, corn starch is employed as a model system to compare linear amylose and highly branched amylopectin on crosslinking and hard carbon anodes. The abundant branch points and amorphous regions of amylopectin facilitate more thorough crosslinking with $(NH_4)_2HPO_4$, forming a denser three-dimensional network. In contrast, dense crystalline domains of amylose restrict crosslinker penetration. These differences dictate the microstructure of carbonized products: high-amylopectin derived hard carbon (A-HC) exhibits smaller interlayer

spacing and higher graphitization, whereas high-amylose derived hard carbon (S-HC) shows larger specific surface area (78.19 $m^2 g^{-1}$) and open porosity (0.0187 $cm^3 g^{-1}$). Electrochemically, A-HC exhibits a reversible capacity of 346.01 mAh g^{-1} alongside an initial Coulombic efficiency of 88.51%, outperforming S-HC (275.67 mAh g^{-1}, 79.97%). Combined with multidimensional in situ characterizations, the sodium storage mechanism follows an adsorption-intercalation/pore filling model. This work establishes a clear structure property relationship linking precursor molecular topology to hard carbon performance, offering new insights for the rational design of biomass-derived hard carbon anodes.

Keywords: hard carbon anode; sodium-ion batteries; precursor structure; starch

1. Introduction

Biomass, as a renewable carbon source, is among the most widely used raw materials for the preparation of hard carbon anode materials. Biomass-derived hard carbon [1] demonstrates excellent overall performance and broad application prospects in sodium-ion batteries [2-4] and related fields. However, the diversity of biomass precursors and their complex molecular structures, characterized by large molecular weights, abundant functional groups, and diverse spatial configurations, result in significant differences and uncertainties in the microstructure (such as porosity, graphite microcrystals, and interlayer spacing) and electrochemical properties of the final carbonized products [5, 6]. Recent studies have therefore focused on rational precursor design, molecular-level regulation, and interfacial electrochemical behaviors to achieve optimized hard carbon properties [7-10]. In particular, precursor molecular structures play a critical role in influencing the microstructure and electrochemical performance of hard carbon. For example, the Maillard reaction between reducing sugars and amino acids enables endogenous N/S co-doping and microstructural tailoring of hard carbon anodes, facilitating the formation of an inorganic-rich SEI layer that accelerates ion transport and suppresses side reactions [11]. In another approach, strategies for compatibilizing and

crosslinking biomass polysaccharides with pitch or coal-based materials enable precise tailoring of the microcrystalline structure and ionic diffusion kinetics of hard carbon [12, 13]. Additionally, directly leveraging the multi-component nature of lignocellulosic biomass (such as bagasse), which contains cellulose, hemicellulose, and lignin, can naturally result in hierarchical porous structures and retention of oxygen-containing functional groups after carbonization, thereby providing abundant active sites for sodium storage [14]. Alternatively, introducing lignin into cellulose precursors can alter the pyrolysis pathway, leading to the construction of rich C=O functional groups and a porous architecture in the resultant carbon structure [15].

Nevertheless, current research predominantly focuses on macroscopic compositional differences among various biomass species or on modifications achieved by introducing exogenous components, while systematic understanding of the intrinsic molecular fine structure within the same biomass species remains limited. Taking starch as an example, studies on starch-derived hard carbon have mainly emphasized the preservation of its spherical morphology and the suppression of melting and foaming, aiming to reduce specific surface area and enhance initial Coulombic efficiency [16]. Despite being polysaccharides, starches from different sources exhibit fundamental differences in degree of polymerization, the ratio of amylose to amylopectin, and crystalline structure [17-20]. However, how these molecular-level structural parameters directly influence crosslinking behavior during pyrolysis, the evolution of the carbon skeleton, and the resulting microstructure of hard carbon has yet to be clearly elucidated.

Diammonium hydrogen phosphate ($(NH_4)_2HPO_4$, DAP) exerts two key regulatory effects on starch matrices. On one hand, DAP serves as an efficient crosslinking agent. It reacts with hydroxyl groups on starch molecular chains to form C-O-P phosphate ester linkages, which construct a stable three-dimensional network structure. This network effectively inhibits the melting and foaming behaviors of starch matrices during the carbonization process. On the other hand, DAP acts as a dual heteroatom dopant source containing nitrogen and phosphorus. It can introduce nitrogen and phosphorus heteroatoms into carbon skeletons, which improves the

electrical conductivity of carbon materials and creates abundant additional active sites for sodium ion storage [21]. Nevertheless, there remains a lack of systematic and in-depth mechanistic research on how typical starch chain architectures (linear structure and highly branched structure) regulate the crosslinking efficiency of DAP, as well as the subsequent evolution of graphitic microcrystallites, closed pore structures, and sodium storage performance. In this study, homologous corn starch is adopted as the model system to systematically compare the differential functions of linear amylose and highly branched amylopectin in the DAP-mediated crosslinking reaction and subsequent carbonization process. Precursors with well-defined molecular topological structures are fabricated and treated under identical crosslinking and carbonization conditions, enabling the establishment of a direct correlation between precursor molecular chain configuration and the electrochemical performance of hard carbon materials. This work specifically clarifies the regulatory mechanism of linear and branched molecular architectures on the density of crosslinking networks, the evolution behavior of graphitic microcrystals and closed pores during carbonization, and the resultant sodium storage kinetics and electrochemical properties. The research findings verify the crucial contribution of branched molecular structures to the fabrication of high-performance hard carbon anodes, providing novel mechanistic insights and reliable experimental evidence for the targeted design and controllable preparation of biomass-derived hard carbon materials.

2. Results and discussion

2.1. Characterization of Precursors and cross-Linked networks

Firstly, a visual distinction between high-amylose starch (A-AM) and high-amylopectin starch (S-AM) was achieved using the iodine coloration reaction (Figure 1a). Starches with high amylose content form helical inclusion complexes with iodine molecules, resulting in a blue color, in contrast, the branched structure of amylopectin hinders the formation of such helices, giving rise to a purple coloration. The structural differences between the two starches are illustrated in Figure S1. Further quantitative analysis of amylose and amylopectin content was performed

using the dual-wavelength colorimetric method. As shown in Figure 1b and Table S1, S-AM exhibits an amylose/amylopectin ratio of 2.4 (787.86 vs. 328.74 mg g^{-1}), while A-AM shows a ratio of 0.14 (105.14 vs. 777.87 mg g^{-1}).

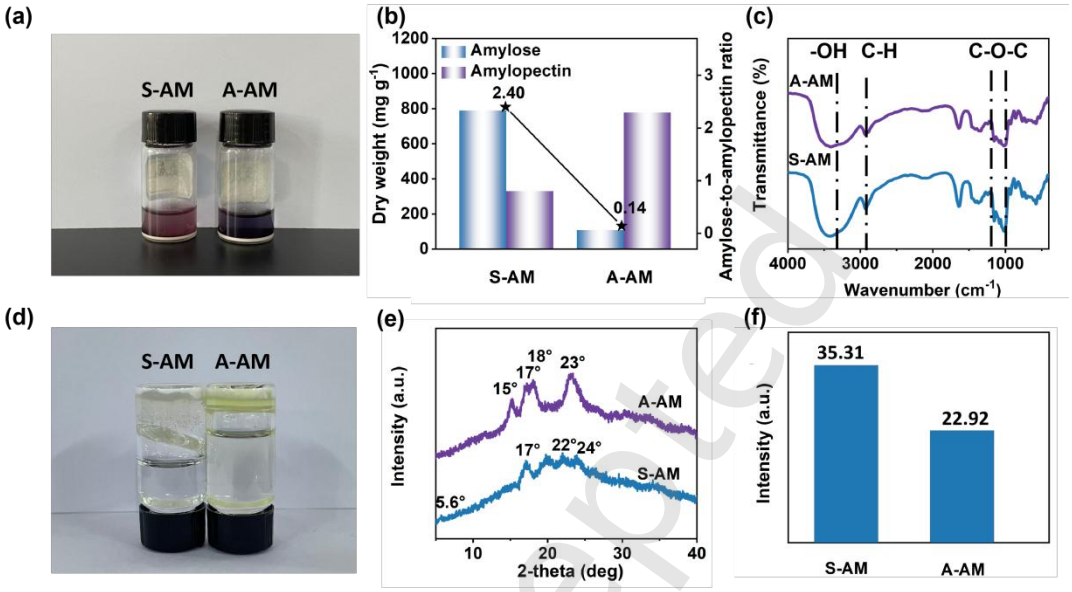

Figure 1. (a) Iodine staining reaction，(b) Quantification of amylose content in starch by dual-wavelength colorimetry, (c) FTIR spectra, (d) Swelling degree test, (e) XRD patterns and (f) Crystallinity fitting of S-AM and A-AM.

The structural differences between the two starches were examined by Fourier-transform infrared (FTIR) spectroscopy (Figure 1c). Their spectra are broadly similar, reflecting their common corn origin. In both cases, a broad band appears near 3416 cm^{-1}, corresponding to -OH stretching vibrations, along with possible minor contributions from water and protein -NH groups [22]. In S-AM, this absorption peak shifts slightly to a higher wavenumber (3429 cm^{-1}), with a narrower and stronger peak shape, indicating enhanced intermolecular hydrogen bonding and greater structural order. The band near 2940 cm^{-1} is assigned to asymmetric C-H stretching of starch [23], while absorptions in the 1000–1200 cm^{-1} region originate from C-O-C and C-O-H stretching in the saccharide ring skeleton [24]. Comparing the spectra, the absorbance of A-AM at 1156 cm^{-1} shifts to a lower wavenumber, while the absorbance at 1020 cm^{-1} moves to a higher wavenumber. These changes are attributed to the rearrangement of the hydrogen bonding network in the molecule, reflecting the dissociation of branched structures and local structural ordering in amylopectin.

The formation and density differences of the cross-linked networks were further verified by swelling degree measurements [25]. As shown in Figure 1d and Figure S2, the swelling degree of A-AM in dimethyl sulfoxide (DMSO) is significantly lower than that of S-AM. This is because the branched structure of amylopectin (S-AM) provides more potential cross-linking sites, resulting in a denser three-dimensional network under identical reaction conditions, with shorter molecular chains (network strands) between cross-link points. This restricts the infiltration and expansion of solvent molecules. These results clearly demonstrate that amylopectin possesses a higher cross-linking density and a more complete network structure.

The crystalline structures of S-AM and A-AM were characterized by X-ray diffraction (XRD) analysis. As shown in Figure 1e, A-AM exhibits typical A-type starch crystallinity [26], with prominent diffraction peaks at approximately 15°, 17°, 18°, and 23°. S-AM, however, presents characteristic B-type starch crystallinity [27] with peaks at 5.6°, 17°, 22°, and 24°. Calculations show that the degree of crystallinity for S-AM is 35.31%, whereas A-AM has a much lower value of 22.92% (Figure 1f). This disparity originates from differences in their molecular chain stacking abilities: S-AM, with its linear molecular structure, readily forms well-ordered and dense double helices via intermolecular hydrogen bonding, resulting in more complete crystallinity. In contrast, the highly branched topology of A-AM impedes long-range order, leading to lower crystalline integrity.

Figure 2 illustrates the structural evolution of S-AM and A-AM during cross-linking with diammonium hydrogen phosphate. As depicted in Figure 2a, under these conditions, the linear starch (S-AM) and branched starch (A-AM) each undergo esterification cross-linking with diammonium hydrogen phosphate, forming three-dimensional network structures. The linear structure of S-AM limits cross-linking sites to chain ends and amorphous regions, while the highly branched structure of A-AM provides a greater abundance of reactive sites, conducive to forming a denser cross-linked network. Specifically, the two types of starch were mixed with diammonium hydrogen phosphate at a mass ratio of 5:1 and subjected to ball milling. XRD analysis (Figure 2b) indicates that both resulting materials (S-BM

and A-BM) display broad, diffuse peaks with no sharp reflections, indicating a transition to a largely amorphous structure. Their crystallinity decreased to 17.89% (S-BM) and 6.99% (A-BM), respectively (Figure 2c). The reduction in crystallinity was 49.30% for S-AM and 69.50% for A-AM, directly reflecting differences in cross-linking efficiency: the greater number of branch points and larger amorphous regions in A-AM provide greater accessibility to reactive sites [28]. In comparison, the dense crystalline domains in S-AM partially hinder the penetration and reactivity of the cross-linking agent, thus retaining some ordered structure.

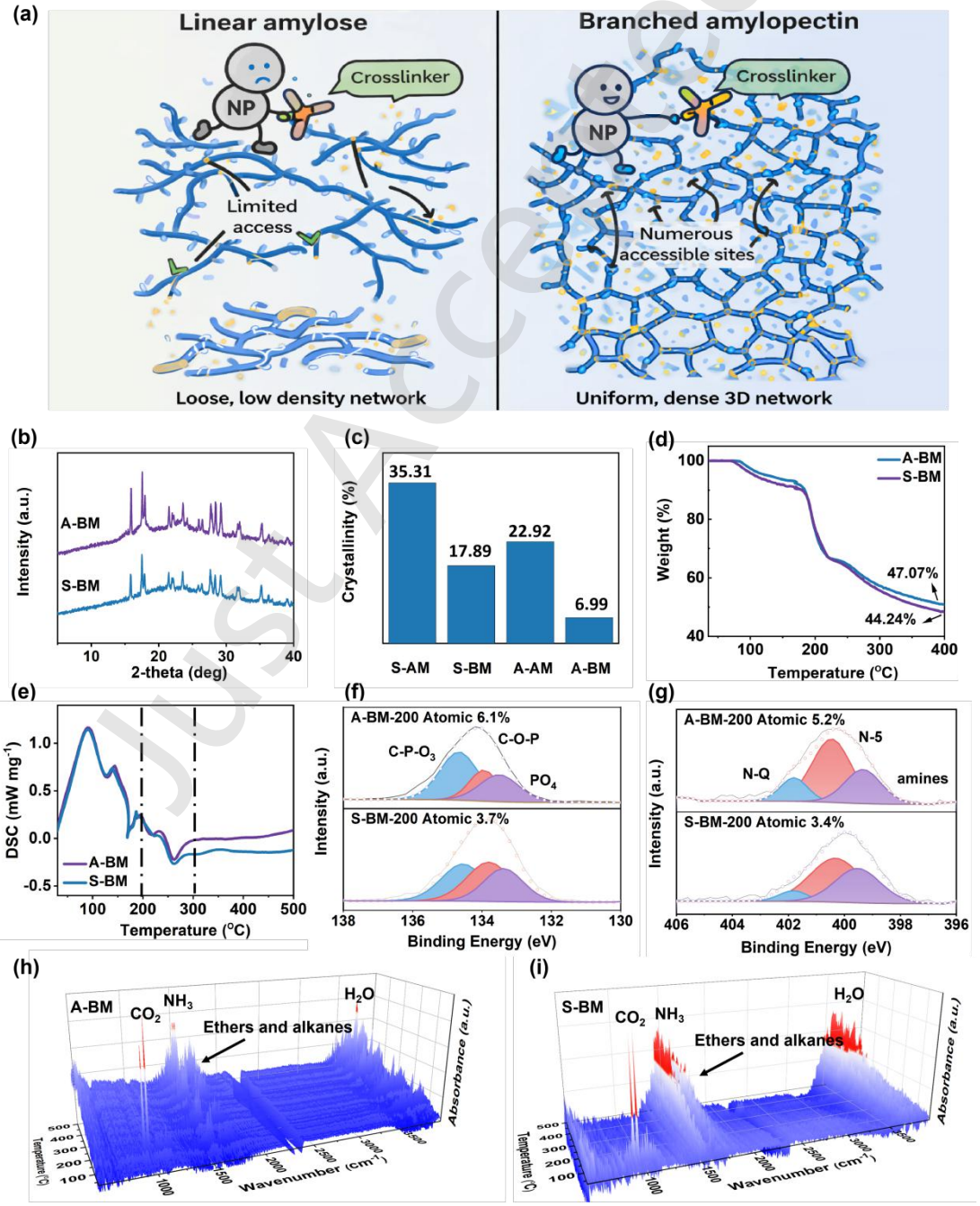

Figure 2. (a) Schematic diagram of crosslinking reaction, (b) XRD patterns and (c) Crystallinity fitting results of S-BM and A-BM. (d) TGA curves, (e) DSC curves of S-BM and A-BM. XPS spectra of (f) P 2p and (g) N 1s of crosslinked samples. (h) TG-FTIR spectra of A-BM and (i) S-BM.

Thermogravimetric analysis (TGA) was further used to compare the thermal behaviors and carbonization characteristics of S-BM and A-BM, the composite systems of high-amylopectin/high-amylose with diammonium hydrogen phosphate. The TGA curves (Figure 2d) show three distinct mass loss stages for both systems: dehydration at low temperature (25-120 °C), primary decomposition at intermediate temperature (120-300 °C), and carbonization stage (300-500 °C) [21, 29]. Notably, the final char yield of the A-BM system is significantly higher than that of S-BM, with the corrected char yields being approximately 47.07% and 44.24%, respectively, indicating that the branched structure is more favorable for phosphate-catalyzed carbonization. Analysis of the derivative thermogravimetric (DTG) curves (Figure S3) further reveals that A-BM exhibits a broader and lower main decomposition peak, suggesting that its thermal degradation occurs over a wider temperature range, effectively suppressing the weight loss rate. Conversely, the main decomposition peak in the S-AM system is sharper, with a higher weight loss rate, indicating a more intense thermal decomposition process.

The DSC results shown in Figure 2e indicate that in the intermediate temperature range (200-300 °C), the S-BM system exhibits a much more intense and concentrated exothermic process, with a deep and sharp exothermic peak, suggesting that the cross-linking and thermal decomposition reactions occur in a locally explosive manner [30-32]. In contrast, the A-BM system shows a broader and gentler exothermic peak, distributed over a wider temperature range, indicating that the branched structure of amylopectin provides more active sites for DAP-catalyzed dehydration cross-linking reactions. This leads to a more thorough and mild reaction, preventing the formation of defects caused by localized intense heat release. Above 300 °C, the A-BM system maintains a slow endothermic process, which corresponds to the aromatization and stabilization of a dense carbon layer. In comparison, the heat

flow signal of the S-BM system becomes stable, suggesting that its carbon layer structure has essentially decomposed and can no longer provide effective thermal stability.

These results demonstrate that under the catalytic action of DAP, the highly branched structure of amylopectin considerably promotes homogeneous cross-linking, resulting in the formation of a continuous, compact, and thermally stable carbonaceous structure. For amylose, the high crystallinity limits DAP diffusion into the molecular chains, restricting cross-linking primarily to the amorphous regions and leading to a relatively loose carbon structure that cannot effectively suppress subsequent thermal decomposition. The surface chemical states of the cross-linked samples were further characterized by X-ray photoelectron spectroscopy (XPS), as shown in Figures 2f, 2g, and S4 . The P 2p spectrum can be fitted into three components: C-P-O_3 (133.5 eV), C-P-O (133.9 eV), and PO_4 (134.5 eV), while the N 1s spectrum features peaks corresponding to amine (399.6 eV), N-5 (400.3 eV), and N-Q (401.8 eV) chemical environments [21, 33]. The P/C and N/C atomic ratios derived from the spectra (Table S2, S3) provide quantitative measures of the crosslinking degree and heteroatom doping level. During the crosslinking process, ammonia interacts with pyrolyzed starch products to form substituted amines/amides, while hydroxyl groups (-OH) of phosphoric acid condense with the side-chain hydroxyl groups of starch decomposition products to form C-O-P bonds, thereby generating additional active hydroxyl sites for further reactions with ammonia and its derivatives. Phosphorus and nitrogen elements function as bridges, becoming integrated into larger molecular units through rearrangement and self-cyclization reactions [21]. Comparing the atomic compositions of P and N in the cross-linked products S-BM-200 and A-BM-200, the atomic percentages are markedly higher in the A-BM-200 sample, indicating that more phosphorus and nitrogen have been retained. Furthermore, elemental analysis (Table S4) confirms that A-AM incorporated higher amounts of N and P during the crosslinking process, with N and P contents of 3.25% and 5.56% in A-BM-200, respectively, compared to 2.81% and 4.70% in S-BM-200. This confirms that the cross-linking between amylopectin and

DAP is more effective, resulting in a more uniformly doped and highly cross-linked 3D network structure.

In situ structural evolution during the programmed heating of cross-linked starches was analyzed by thermogravimetry-infrared (TG-IR) spectroscopy (Figures 2h and 2i). In the initial pyrolysis stage below about 250 °C, the predominant released gases are CO_2 (infrared band at ~2350 cm^{-1}) and small molecules containing C=O such as aldehydes, ketones, and esters (peaks around 1750 cm^{-1}). At this stage, the material begins to form a porous, multifunctional carbon precursor structure. From 200 °C, NH_4^+ from the cross-linker starts to evolve as NH_3, and at temperatures above 250 °C, CO (around 2200 cm^{-1}) becomes the main gaseous product, accompanying further pore development. In addition, the release of phenolic compounds from C-OH (1300-1400 cm^{-1}), as well as carboxylic acids, alcohols, and esters containing C-O bonds, was identified [34]. Notably, the S-BM cross-linked product continues to release gases near 600 °C, indicating its cross-linked network has lower thermal stability and a weaker degree of cross-linking.

The differences in cross-linking behavior originate from the distinct molecular topologies of amylose and amylopectin. Amylose, as a linear polysaccharide, has regular chain packing and readily forms dense crystalline domains by intermolecular hydrogen bonding. This ordered structure partially impedes the diffusion and uniform distribution of DAP, causing cross-linking to occur mainly in the amorphous regions and on the particle surface. As a result, the resulting 3D network generally has lower cross-linking density and higher structural heterogeneity. In contrast, the highly branched topology of amylopectin provides abundant chain ends and amorphous regions, markedly enhancing the accessibility of reactive sites. The branch points serve as hubs for multidimensional cross-linking and facilitate uniform penetration and reaction of the cross-linker within the molecular structure during thermochemical processing. Consequently, a denser distribution of cross-link points and a more ideal network topology are achieved. These topology-driven differences in cross-linking behavior directly affect the precursor network's cross-linking density and thermal stability [35].

2.2. Hard carbon microstructure

Figure 3 presents the microstructure and pore characteristics of hard carbons derived from amylose (A-HC) and amylopectin (S-HC) precursors. Raman spectroscopy analysis reveals that both hard carbon materials exhibit typical carbon-related features, including the D band at 1343 cm^{-1} and the G band at 1590 cm^{-1}. The degree of disorder in the hard carbon can be assessed by the relative intensity of the D band to the G band, where the G band corresponds to the graphitic layered structure with sp^2 hybridization [36]. Peak fitting calculations indicate that the I_D/I_G ratio of S-HC is slightly higher than that of A-HC, implying a higher defect density within S-HC (Figure 3a). X-ray diffraction (XRD) patterns indicates that both materials exhibit a broad (002) reflection at approximately 23°. Notably, the peak for A-HC shifts to a higher angle, and a pronounced (100) graphite feature appears near 80°, indicating a higher degree of graphitic ordering in A-HC (Figure 3b). Calculated microcrystalline parameters are displayed in Figure 3c， the lateral size (La) for S-HC and A-HC are 3.59 nm and 4.73 nm, respectively, while the stacking height (Lc) are 1.98 nm (S-HC) and 2.59 nm (A-HC). The anisotropy La/Lc values are 1.81 and 1.83 (A-HC), respectively (Figure S5 and Table S5), suggesting that the higher cross-linking density of the amylopectin precursor, S-HC tends to form larger and thicker microcrystals with increased lateral dimensions after carbonization [37].

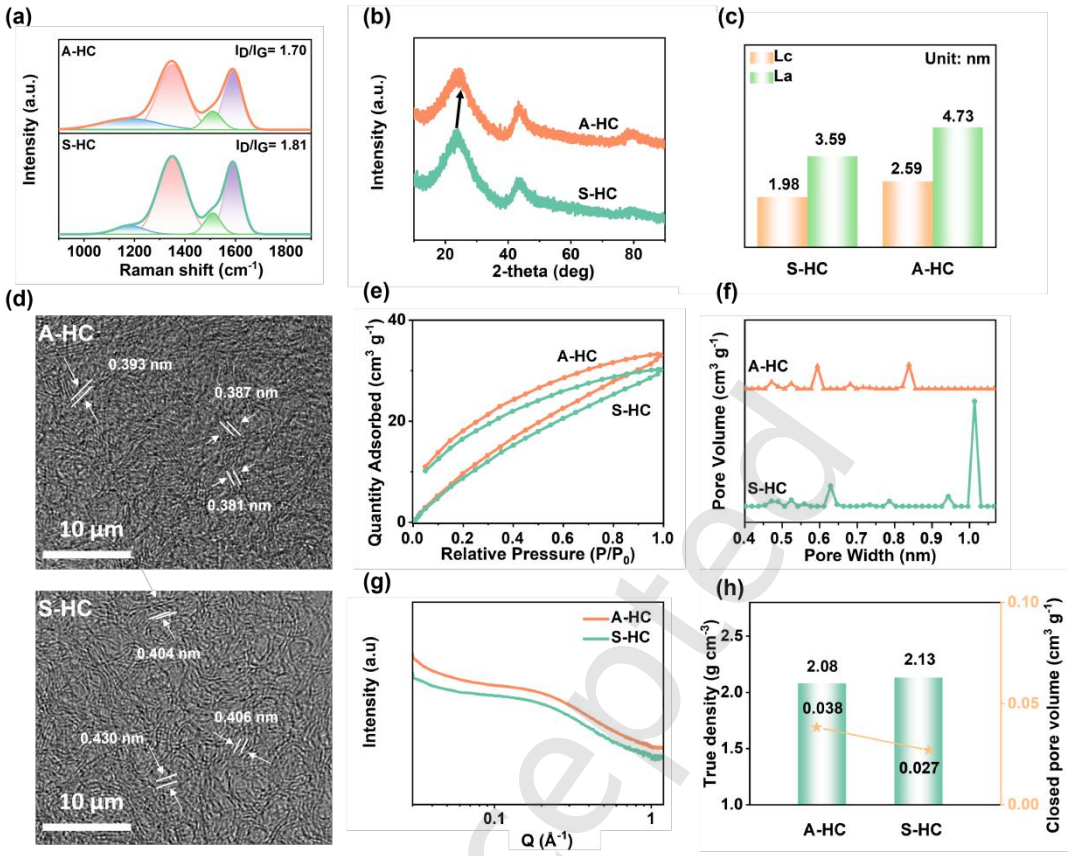

Figure 3. (a) Raman spectra; (b) XRD patterns, (c) Microcrystalline parameters, (d) HRTEM images, (e) CO_2 adsorption-desorption isotherms, (f) pore size distribution curves, (g) SAXS patterns, (h) True density and closed pore volume values of A-HC and S-HC.

High-resolution transmission electron microscopy (HRTEM) observations (Figure 3d) demonstrate that the interlayer spacings of the (002) plane in A-HC are 0.381 nm, 0.387 nm, and 0.393 nm, all smaller than those of S-HC (0.404 nm, 0.406 nm, and 0.430 nm), directly confirming that A-HC has a higher graphitization degree and a more densely packed multilayer carbon structure. To comprehensively characterize the porous structure of the two hard carbon materials, complementary N_2 and CO_2 adsorption measurements were performed. N_2 adsorption is well-suited for quantifying open micropores (>0.7 nm) and mesopores. As displayed in Figure S6, S-HC delivers a higher specific surface area of 78.19 $m^2\ g^{-1}$ than A-HC (63.08 $m^2\ g^{-1}$), along with a larger total pore volume (0.0187 $cm^3\ g^{-1}$ for S-HC versus 0.0063 $cm^3\ g^{-1}$ for A-HC). These results suggest that the less efficient crosslinking of the amylose precursorpromotes greater gas release during carbonization, thereby generating more

developed open porosity in S-HC. In comparison, CO_2 adsorption serves as an effective probe for ultramicropores (<0.7 nm) [38]. As illustrated in Figures 3e and 3f, the CO_2 adsorption-desorption isotherms confirm the abundant ultramicropores in A-HC. Such structural characteristics stem from the dense carbon network derived from the highly crosslinked amylopectin precursor. Small-angle X-ray scattering analysis (Figure 3g) further reveals that A-HC displays much stronger scattering intensity in the low-Q region, with corresponding 2D images clearly showing the difference in diffraction intensity (Figure S7), indicating that A-HC possesses a greater abundance of closed pores. The high-density cross-linked network in amylopectin acts as a cage that restricts the free rearrangement and shrinkage of carbon layers. Upon carbonization, the carbon layers primarily stack within nanoscale-confined spaces, forming curved and closed carbon layer structures, these curved carbon layers themselves forming the closed pore framework. True density analysis offers further evidence for identifying closed pores. As shown in Figure 3h and Table S6, A-HC exhibits the lowest true density among the two samples. Comparing these values with those of graphite allows estimation of the closed pore volume within hard carbon materials [39], with A-HC showing the largest closed pore volume (0.038 $cm^3 g^{-1}$ for A-HC and 0.027 $cm^3 g^{-1}$ for S-HC).

Scanning electron microscopy (SEM) images (Figure S8) indicate that A-HC largely retains the spherical morphology of the starch precursor, with clear particle contours and well-defined structures, whereas S-HC exhibits more amorphous carbon characteristics, including blurred particle boundaries and a less compact structure. This morphological difference is closely related to their electrochemical performance: the regular, spherical structure of A-HC facilitates the formation of a stable electrode/electrolyte interface, reduces side reactions, and hence delivers superior electrochemical performance and higher initial coulombic efficiency [40].

2.3. Electrochemical performance

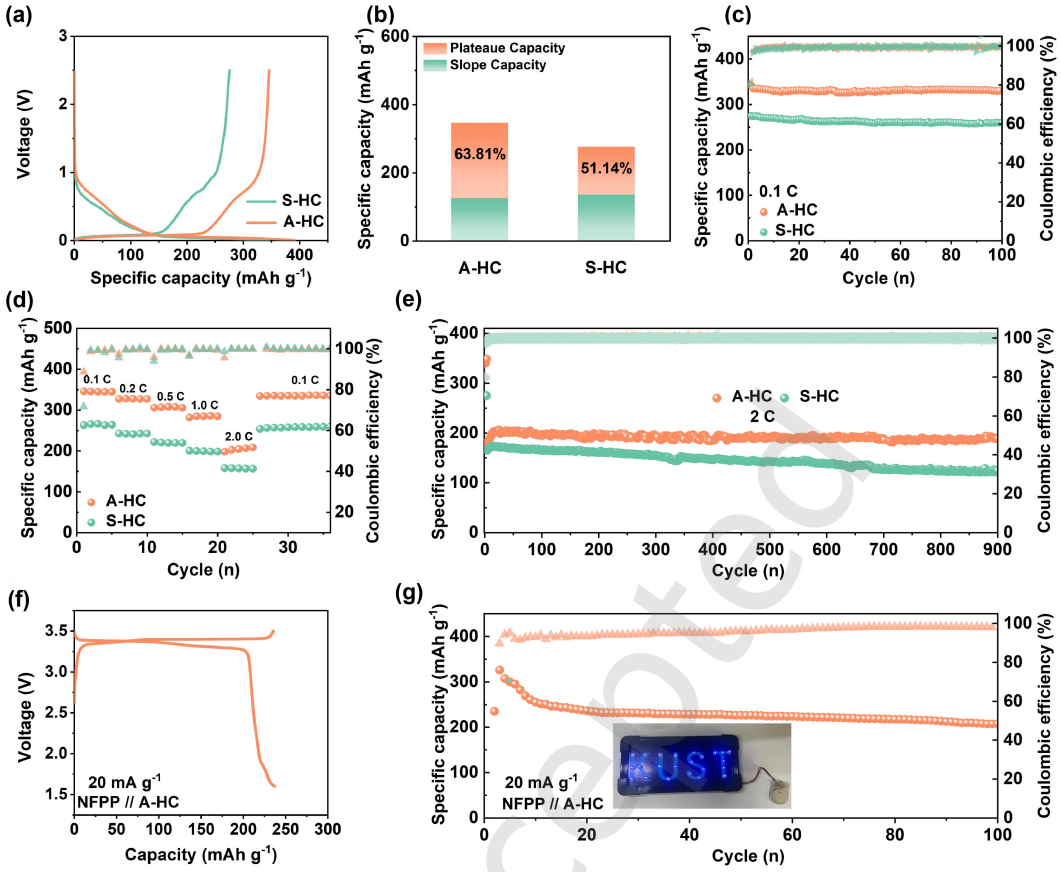

Figure 4. (a) The galvanostatic charge-discharge curves of A-HC and S-HC at 0.1 C. (b) Slope region and plateau region capacity contributions. (c) Long-term cycling performance at 0.1 C, (d) Rate performance and (e) Long-term cycling performance at 2 C of A-HC and S-HC. (f) The charge-discharge curve and and (g) Long-term cycling performance of full cell.

As shown in Figure 4a, during the first charge/discharge cycle at 0.1 C, A-HC delivers a reversible specific capacity of 346.01 mAh g^{-1} with an initial coulombic efficiency of 88.51%, compared to 275.67 mAh g^{-1} and 79.97% for S-HC. A comparison of the electrochemical performance of biomass-derived hard carbon with previously reported materials is provided in Table S7. The proportions of plateau capacity and sloping-region capacity of the two samples are summarized in Figure 4b, while the correlation between plateau capacity and closed-pore volume is illustrated in Figure S9. The higher graphitization degree of A-HC promotes the formation of more ordered carbon layer stacks during carbonization. Owing to the high crosslinking density inherited from the amylopectin precursor, these ordered stacks tend to curve and close at their edges, forming closed pores. Consequently, A-HC

exhibits a higher plateau capacity. After 100 cycles (Figure 4c), the capacity of A-HC remains at 330.4 mAh g^{-1}, while S-HC maintains 259.8 mAh g^{-1}, indicating good cycling stability for both materials. In rate performance tests (Figure 4d), A-HC retains a reversible capacity of 208.60 mAh g^{-1} at a current density of 2 C, which is significantly superior to that of S-HC (156.80 mAh g^{-1}). Under a 2 C current density (Figure 4e), both materials undergo an activation process for roughly 10 cycles, after which the capacities stabilize at 190.20 mAh g^{-1} (A-HC) and 124.82 mAh g^{-1} (S-HC) over 900 cycles. Long-term cycling tests confirm that A-HC exhibits superior cyclic stability, attributed to its more regular spherical morphology, higher degree of graphitization, and more stable cross-linked carbon framework, which together facilitate rapid sodium-ion diffusion and charge transfer.

As shown in Figure 4f, a full cell was assembled using an A-HC anode and a $Na_4Fe_3(PO_4)_2P_2O_7$ (NFPP) cathode, with a negative-to-positive capacity (N/P) ratio of 2:1. The full cell maintains good capacity after 100 stable cycles at 20 mA g^{-1} (Figure 4g) and can power an LED display, demonstrating the practical application potential of the A-HC anode.

2.4. Sodium storage behavior

Systematic electrochemical kinetics analyses of both hard carbons were performed to obtain further insight into their sodium storage behaviors. Their cyclic voltammetry (CV) curves at the same scan rate (0.1 mV s^{-1}) show that A-HC exhibits stronger redox peaks and a larger enclosed area (Figure S10). The capacitive and diffusion-controlled contributions were quantified by CV at varying scan rates (Figures 5a, 5b, S11), yielding b-values of 0.62 (S-HC) and 0.58 (A-HC) (Figure 5c). Based on kinetic analysis, sodium storage in the two materials proceeds through both diffusion-controlled and surface pseudocapacitive behaviors, but the contribution from diffusion is relatively higher in A-HC (Figures 5d and 5e). This observation is likely attributable to its higher degree of graphitization and abundant closed pores, which contribute to pronounced diffusion-controlled sodium storage [41]. The initial electrochemical impedance spectra (EIS) in Figure 5f reveal that A-HC exhibits a smaller charge transfer resistance (Rct = 199.31 Ω) compared to S-HC (289.92 Ω),

confirming its enhanced ionic conductivity and accelerated reaction kinetics. This accounts for the superior capacity retention of A-HC. The equivalent circuit used for impedance fitting is shown in Figure S12, and the corresponding fitting parameters are listed in Table S8. Galvanostatic intermittent titration technique (GITT) measurements (Figures 5g and 5h) further reveal that the Na^+ diffusion coefficient (D_{Na}) for both materials decreases dramatically during sodium insertion and reaches a minimum around 0.01 V. This suggests that electrochemical reaction kinetics are slower in the plateau region below 0.1 V, as sodium storage here mainly occurs via Na^+ deposition into closed nanopores [42]. Notably, A-HC delivers a higher D_{Na} than S-HC, which is highly consistent with its well-ordered carbon layer structure and shortened ion diffusion pathways.

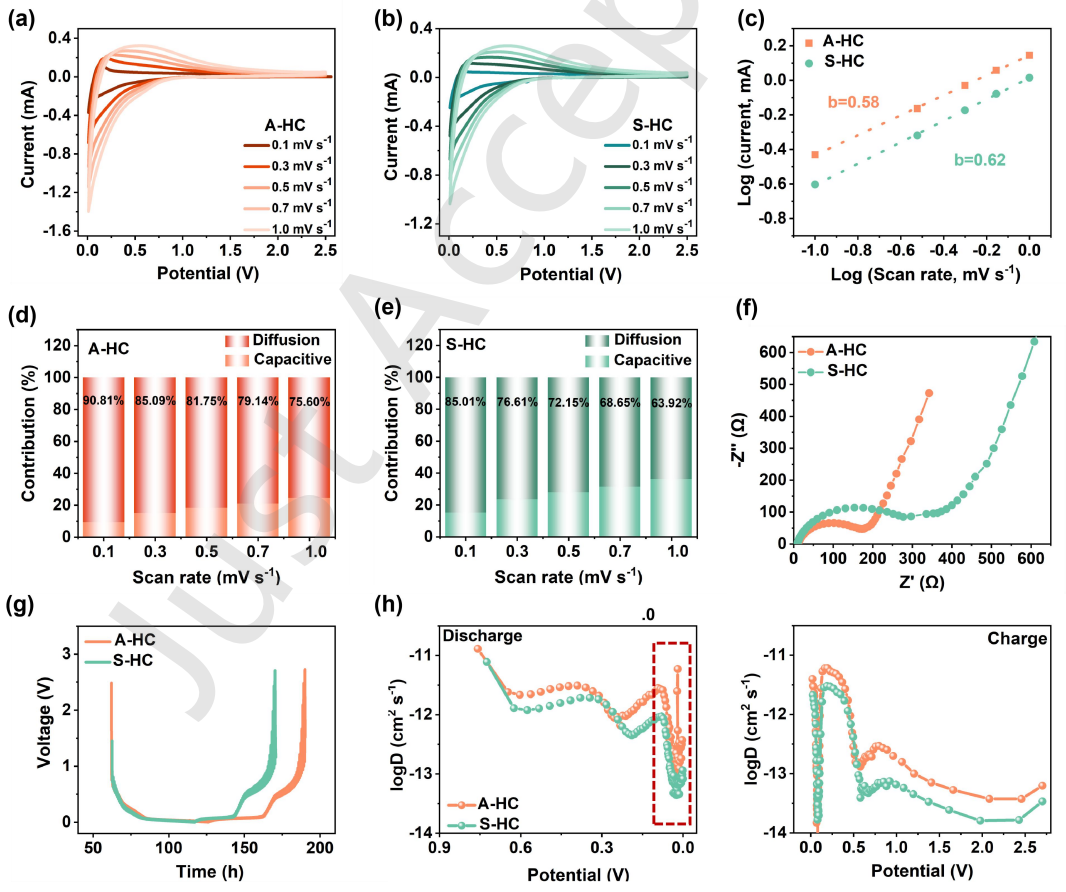

Figure 5. (a) CV curves of A-HC and (b) S-HC at different scan rates. (c) Plots of log v versus log i. (d) Capacitive-diffusion controlled contribution distribution of A-HC and (e) S-HC. (f) Nyquist plots, (g) GITT curves, (h) The variation of calculated Na^+ diffusion coefficients against different potentials at discharge and charge processes.

In situ electrochemical impedance spectroscopy (EIS) during the first cycle shows that A-HC exhibits lower solution and charge transfer resistances (Figure 6a), confirming its faster ion transport kinetics. Distribution of relaxation time (DRT) analysis (Figures 6b and 6c) provides a quantitative assessment of these kinetic processes. The τ_1 peak, corresponding to SEI and interface resistance in the mid- to high-frequency region, is consistently lower for A-HC throughout charge–discharge, indicating that A-HC forms a more stable and lower-resistance solid electrolyte interphase (SEI). This is mainly attributed to A-HC's lower specific surface area and predominantly closed-pore structure , with fewer open pores to suppress excessive electrolyte decomposition. In addition, the resistance τ_2 associated with Na^+ diffusion is also lower for A-HC compared to S-HC, indicating reduced polarization and faster charge transfer during Na^+ insertion/extraction, which is consistent with its superior rate performance [43].

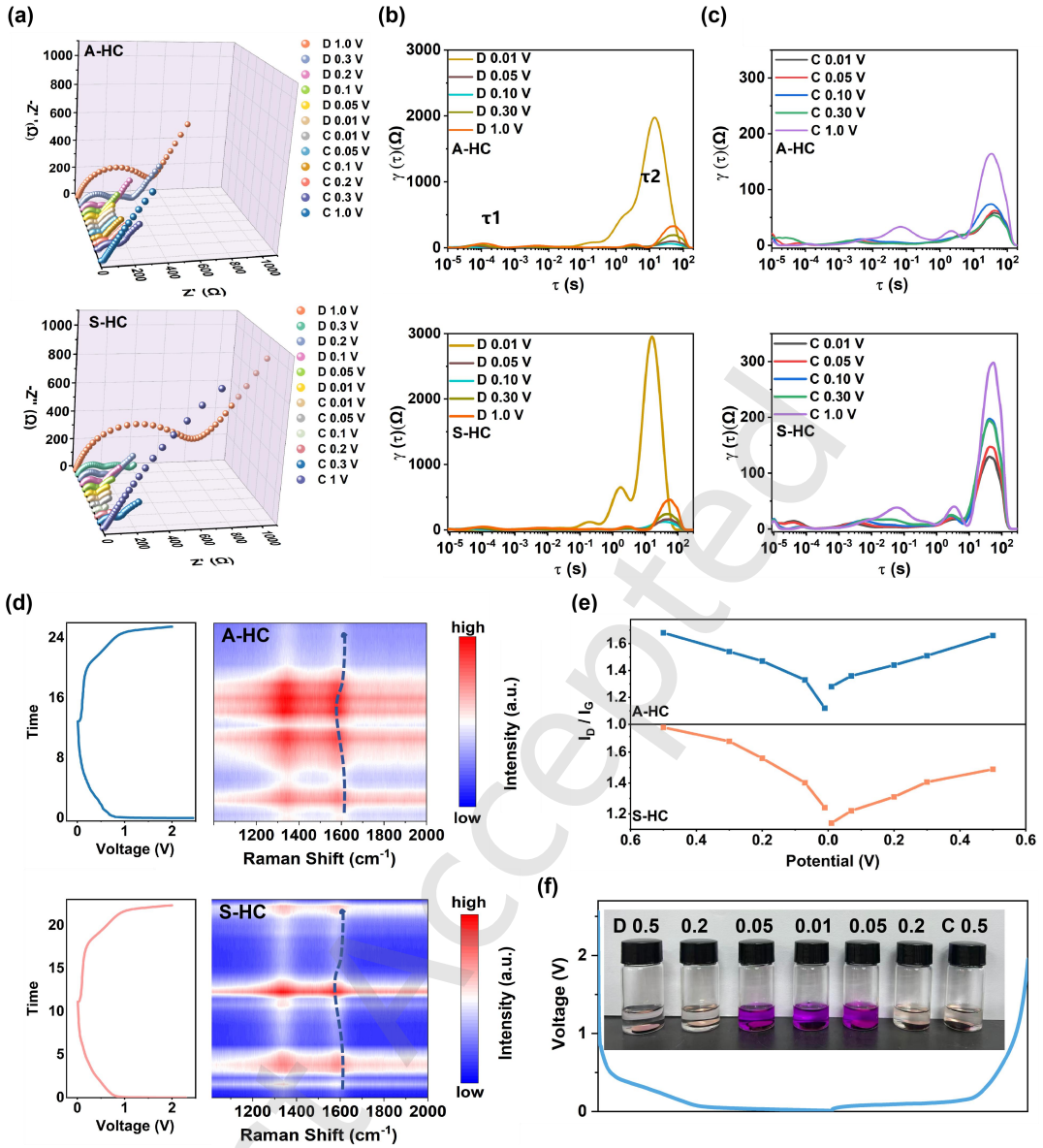

Figure 6. (a) In situ Nyquist plots, (b) DRT spectra of A-HC and S-HC during (b) discharge and (c) charge. (d) In situ Raman spectra, (e) Defect degree during charge-discharge processes. (f) Color change of ethanol-phenolphthalein solution after reaction with A-HC at different potentials.

The sodium storage mechanism was further investigated by in situ Raman spectroscopy (Figure 6d), which monitored the carbon structure upon cycling. The invariance of the D-band position suggests that the sloping-region Na^+ storage is dominated by adsorption. In the plateau region (0.1-0.01 V), however, the G band downshifts, likely due to electron localization on the π* band of the carbon layers [44], leading to Na-C interaction and coupling. Upon desodiation, the G band gradually

returns to its initial position [45]. Furthermore, the accumulation of Na^+ within closed pores can induce local structural rearrangement, resulting in a pronounced decrease in the D-to-G band intensity ratio (I_D/I_G) in the low-potential region, as shown in Figure 6e. Upon sodiation to 0.01 V, sodium ions are deposited into closed nanopores, forming quasi-metallic sodium clusters [46]. This sodium clustering induces localized strain and electron redistribution within the carbon layers, temporarily altering the resonance conditions of the D and G bands and thus reducing the I_D/I_G ratio. During desodiation, as sodium clusters are removed from the closed pores, the carbon layers relax back to their original configuration, and the I_D/I_G ratio returns to near its initial value. This reversibility is supported by the nearly identical I_D/I_G ratios observed before sodiation and after full desodiation. HRTEM images of A-HC after discharge to 0.01 V show in Figure S13 dispersed dark-contrast clusters, which can be ascribed to the formation of sodium clusters. The color change observed when ethanol-phenolphthalein solution is brought into contact with A-HC electrodes at different voltages (Figure 6f) further supports this: following discharge to 0.01 V, the solution turns pink, indicating the generation of active sodium species at the electrode surface; in contrast, electrodes discharged to 0.2 V or after charging show no obvious color change, further confirming sodium cluster formation in closed pores at low potential and their reactivity with ethanol to produce sodium ethoxide. Overall, both hard carbons exhibit a typical multi-stage "adsorption-intercalation/pore filling" sodium storage mechanism during sodiation/desodiation.

3. Conclusions

In this study, corn starch was used as a model precursor to elucidate how molecular topology differences between amylose and amylopectin affect cross-linking behavior, as well as the structure and performance of derived hard carbon anodes. The highly branched structure of amylopectin provides abundant reactive sites, leading to more complete cross-linking with diammonium hydrogen phosphate (DAP) and a denser three-dimensional network. In contrast, the dense crystalline regions of amylose restrict cross-linker penetration, resulting in lower cross-linking degree. This

divergence subsequently determines the microstructure of carbonized products. The highly cross-linked network of amylopectin acts as a directional template during carbonization: compact cross-linking points confine carbon layer expansion, promoting ordered stacking in confined space, thereby yielding smaller interlayer spacing, higher graphitization, and more abundant closed pores. By contrast, the loosely cross-linked network in amylose provides limited constraint, resulting in larger interlayer spacing, lower graphitization, and more open pores. Electrochemical tests show that A-HC achieves a reversible capacity of 346.01 mAh g^{-1} and initial Coulombic efficiency of 88.51% at 0.1 C, both superior to S-HC, along with higher Na^+ diffusion coefficients and better cycling stability. The innovation lies in establishing a systematic structure property relationship from starch molecular topology, through cross-linking behavior, to hard carbon microstructure and electrochemistry. This study clarifies the crucial role of branched structures in constructing high performance hard carbon anodes, providing new theoretical insight and experimental support for rational design of biomass-derived hard carbons.

Conflict of interest

The authors declare no conflict of interest.

Data Availability Statement

The data that support the findings of this study are available from the corresponding author upon reasonable request.

Acknowledgements

This contribution is mainly supported by the National Natural Science Foundation of China (Grant No.52574403), Natural Science Foundation of Yunnan Province (202501AS070125), Quzhou Municipal Science and Technology Program (No. 2025K166), Key Research and Development Program of Yunnan Province (202403AA080018) and Scientific and Technological Project of Yunnan Precious Metals Laboratory (YPML-20240502015).

References

[1] Zhu, Z.; Men, Y.; Zhang, W.; Yang, W.; Wang, F.; Zhang, Y.; Zhang, Y.; Zeng, X.; Xiao, J.; Tang, C.; Li, X.; Zhang, Y. Versatile carbon-based materials from biomass for advanced electrochemical energy storage systems. *eScience* **2024**, *4*, 100249.

[2] Yang, Y.; Zhou, S.; Zhang, Y.; Zhou, Y.; Li, H.; Chen, Y.; Liu, Y.; Cao, P.; Lin, S.; Pan, A. Charge redistribution and local crystal reconstruction in Fe-based polyanion cathodes towards all-climate sodium-ion batteries. *Energy Storage Materials* **2026**, *86*, 104968.

[3] Li, M.; Liu, Z.; Zhao, Y.; Chen, Z.; Zhang, Y.; Zhang, N. Enhanced sodium storage in hard carbon via solvent co-intercalation electrolyte enabling Ah-level pouch cells at low temperatures. *Nature Communications* **2026**, *17*, 1478.

[4] Yang, Y.; Zhou, S.; Li, H.; Zhang, Y.; Liu, Y.; Yuan, Z.; Zong, Q.; Ji, X.; Pan, A. Tailoring Local Electronic Configuration of $Na_4Fe_3(PO_4)_2P_2O_7$ Cathode via Reductive Coupling Mechanism toward Ultra-Wide Temperature Sodium-Ion Batteries. *Advanced Functional Materials* **2026**, e76999.

[5] Lin, J.; Ding, X.; Zeng, X.; Li, Y.; Xiong, X. Interfacial Radical Reaction Enables High-Performance Graphite Anode for Potassium-Ion Batteries. Angewandte Chemie International Edition 2026, 65, e23259.

[6] Ji, C.; Zhou, Q.; Yuan, Y.; Chen, W.; Hou, T.; Zhao, B.; Qin, Y.; Xiong, X. Electron-deficient sites on boron-doped graphite enable air-stable and durable red phosphorus anode for lithium-ion batteries. *Energy & Environmental Science* **2024**, *17*, 4273-4282.

[7] Wang, Y.; Li, M.; Zhang, Y.; Zhang, N. Hard carbon for sodium storage: Mechanism and performance optimization. *Nano Research* **2024**, *17*, 6038-6057.

[8] Li, M.; Sun, C.; Zhang, R.; Qi, M.; Wu, Z.; Zhang, X.; Zhang, Y.; Yuan, J.; Zhang, N. Unveiling the Electrolyte and Solid Electrolyte Interphase in Sodium Ion Batteries: Mechanisms, Progress, and Perspectives. *Advanced Materials* **2025**, *37*, e10882.

[9] Li, M.; Wang, Y.; Zhang, Y.; Zhang, N. Molecular tailoring of biomass precursor to regulate hard carbon microstructure for sodium ion batteries. *Chemical Engineering Journal* **2025**, *506*, 160083.

[10] Qin, S.; You, D.; Wu, X.; Yang, W.; Yu, Y.; Xin, W.; Zhu, Z.; Liu, F.; Li, X. Balancing the "disordered-ordered" microcrystalline structure to achieve high-performance of bituminous coal-based hard carbon anode for sodium-ion batteries. *Journal of Energy Storage* **2026**, *166*, 122411.

[11] Li, H.; Zhou, Y.; Yang, Y.; Chen, Y.; Zhang, Y.; Wang, Z.; Zong, Q.; Fang, G.; Zhou, S.; Pan, A. Manipulating Interphase Chemistry by Endogenous Doping Toward High-Performance Hard Carbon Anodes for Sodium-Ion Batteries. *Nano-Micro Letters* **2026**, *18*, 276.

[12] Lei, Z.; Xiao, S.-H.; Ran, Z.; Liu, S.; Su, X.; Guo, Y.; Li, W.; Li, Q.; Xu, S.; Yin, Y.; Guo, Y. Circumventing Self-Diffusion Enables High-Rate Hard Carbon Anodes. *Advanced Materials* **2026**, *38*, e13193.

[13] Chen, H.; Sun, N.; Zhu, Q.; Soomro, R. A.; Xu, B. Microcrystalline Hybridization Enhanced Coal-Based Carbon Anode for Advanced Sodium-Ion Batteries. *Advanced Science* **2022**, *9*, 2200023.

[14] Kuang, Y.; Zhang, B.; Fan, Y.; He, X.; Hwang, J.; Zhou, D. Bagasse-Derived Hard Carbon Anode with a Synergistic Sodium Storage Mechanism Induced by Temperature Gradient for High-Performance Sodium-Ion Batteries. *Small* **2026**, *22*, e13253.

[15] Lin, P.; Wang, L.; Chen, J.; Fu, H.; Wang, X.; Zhong, Y.; Tu, J. Ultramicropore Engineering Bridges the Capacity-Kinetics Gap in Hard Carbon for Sodium-Ion Battery. *Advanced Energy Materials* **2026**, *16*, e70935.

[16] Huang, J.; Liu, S.; Li, E.; Dai, B.; Lu, T.; Teng, J.; Wu, Y.; Tang, X.; Lei, L.; Yin, D.; Zhang, K.; Li, J. Double functionalization strategy: Using acetate metal salt as medium to optimize hard carbon. *Carbon* **2025**, *234*, 119981.

[17] Deng, N.; Yang, H.; Li, Y.; Zhu, S.; Huang, D. Different starch-mediated modulation of digestibility disparities between whey and casein proteins: Multiscale structural and interaction mechanism investigations. *Food Hydrocolloids* **2026**, *174*, 112403.

[18] Fan, Y.; Xue, L.; Shang, M.; Gao, S.; Zhao, N.; Zhai, H.; He, S.; Zhang, H.; Liu, Q. Natural allelic variation of NAC transcription factor 22 regulates starch biosynthesis and properties in sweetpotato. *Journal of Integrative Plant Biology* **2025**, *67*,

1879-1894.

[19] Yu, T.; Wang, Z.; Yang, X.; Li, Y.; Tian, X.; Rao, L.; Wang, Y.; Liao, X. Interaction between amylose/amylopectin and polyphenols of different structures. *Carbohydrate Polymers* **2025**, *367*, 123976.

[20] Zhiguang, C.; Haixia, Z.; Min, C.; Fayong, G.; Jing, L. The fine structure of starch: a review. *npj Science of Food* **2025**, *9*, 50.

[21] Li, M.; Bi, Z.; Xie, L.; Sun, G.; Liu, Z.; Kong, Q.; Wei, X.; Chen, C. From Starch to Carbon Materials: Insight into the Cross-Linking Reaction and Its Influence on the Carbonization Process. *ACS Sustainable Chemistry & Engineering* **2019**, *7*, 14796-14804.

[22] Sun, Q.; Li, G.; Dai, L.; Ji, N.; Xiong, L. Green preparation and characterisation of waxy maize starch nanoparticles through enzymolysis and recrystallisation. *Food Chemistry* **2014**, *162*, 223-228.

[23] Shi, A.; Wang, L.; Li, D.; Adhikari, B. The effect of annealing and cryoprotectants on the properties of vacuum-freeze dried starch nanoparticles. *Carbohydrate Polymers* **2012**, *88*, 1334-1341.

[24] Fang, J. M.; Fowler, P.; Tomkinson, J.; Hill, C. A. S. Preparation and characterisation of methylated hemicelluloses from wheat straw. *Carbohydrate Polymers* **2002**, *47*, 285-293.

[25] Lee, J. H.; You, S.; Kweon, D.;Chung, H.; Lim, S. Dissolution behaviors of waxy maize amylopectin in aqueous-DMSO solutions containing NaCl and CaCl2. *Food Hydrocolloids* **2014**, *35*, 115-121.

[26] Zhu, J.; Gao, Y.; Li, X.; Lu, C.; Zhou, X.; Chen, L.; Qiu, C.; Jin, Z.; Long, J. Preparation of branched starch by α-amylase and thermophilic glycogen branching enzyme modification. *Food Chemistry* **2025**, *493*, 145748.

[27] Vamadevan, V.; Blennow, A.; Buléon, A.; Goldstein, A.; Bertoft, E. Distinct Properties and Structures Among B-Crystalline Starch Granules. *Starch - Stärke* **2018**, *70*, 1700240.

[28] Bertoft, E. Understanding Starch Structure: Recent Progress. *Agronomy* **2017**, *7*, 56.

[29] Lin, J.; Liao, Z.; Liu, Y.; Zhao, B.; Wang, J.; Xiong, X. Weakly Aggregated Polymeric

Network Enabling Advanced Hard Carbon for Sodium Storage. *Advanced Functional Materials* **2026**, *36*, e76044.

[30] Vamadevan, V.; Bertoft, E. Structure-function relationships of starch components. *Starch -Stärke* **2015**, *67*, 55-68.

[31] Kou, T.; Gao, Q. A study on the thermal stability of amylose-amylopectin and amylopectin-amylopectin in cross-linked starches through iodine binding capacity. *Food Hydrocolloids* **2019**, *88*, 86-91.

[32] Sukhija, S.; Singh, S.; Riar, C. S. Effect of oxidation, cross-linking and dual modification on physicochemical, crystallinity, morphological, pasting and thermal characteristics of elephant foot yam (Amorphophallus paeoniifolius) starch. *Food Hydrocolloids* **2016**, *55*, 56-64.

[33] Bhawana, K.; Gautam, M.; Mishra, G. K.; Chakrabarty, N.; Wajhal, S.; Kumar, D.; Dutta, D. P.; Mitra, S. Endorsing Na^+ storage mechanism in low tortuosity, high plateau capacity hard carbon towards development of high-performance sodium-ion pouch cells. *Carbon* **2023**, *214*, 118319.

[34] Hu, X.; Ji, Y.; Wu, S.; Li, S.; Shi, Q.; Sun, J.; Wan, J.; Zhao, Y. Mass-Transfer Engineered Synthesis of Pitch-Derived Hard Carbons for Enhanced Sodium Storage. *Advanced Energy Materials* **2026**, *16*, e04973.

[35] Liu, X.; Wang, J.; Zhang, B.;Zhang, G.; Li, K.; Guan, T. Programming closed pores in hard carbon: from molecular topology to chemomechanical carbonization. *Energy Storage Materials* **2026**, *88*, 105073.

[36] Zhu, Z.; Men, Y.;Zhang, W.; Guo, Y.; Zeng, X.; Zhang, Y.; Tang, C.; Li, X.; Zhang, Y. Revisiting the Enhancement Mechanism of Electrochemical Performance of Functional Atom-Doped Hard Carbon in Potassium-Ion Batteries. *SusMat* **2025**, *5*, e70017.

[37] Feng, X.; Li, Y.; Li, Y.; Liu, M.; Zheng, L.; Gong, Y.; Zhang, R.; Wu, F.; Wu, C.; Bai, Y. Unlocking the local structure of hard carbon to grasp sodium-ion diffusion behavior for advanced sodium-ion batteries. *Energy & Environmental Science* **2024**, *17*, 1387-1396.

[38] Cazorla-Amorós, D.; Alcañiz-Monge, J.; Linares-Solano, A. Characterization of

Activated Carbon Fibers by CO_2 Adsorption. *Langmuir* **1996**, *12*, 2820-2824.

[39] Lin, J.; Zhou, Q.; Liao, Z.; Chen, Y.; Liu, Y.; Liu, Q.; Xiong, X. Steric Hindrance Engineering to Modulate the Closed Pores Formation of Polymer-Derived Hard Carbon for High-Performance Sodium-Ion Batteries. *Angewandte Chemie International Edition* **2024**, *63*, e202409906.

[40] Yan, L.; Wang, J.; Ren, Q.; Fan, L.; Liu, B.; Zhang, L.; He, L.; Mei, X.; Shi, Z. In-situ graphene-coated carbon microsphere as high initial coulombic efficiency anode for superior Na/K-ion full cell. *Chemical Engineering Journal* **2022**, *432*, 133257.

[41] Liao, Z.; Lin, J.; Li, T.; Liu, Y.; Xiong, X. Suppressing Lignin Self-Condensation Enables Microstructure Engineering of Bamboo Derived Hard Carbon for High Performance Sodium-Ion Batteries. *Small* **2026**, *22*, e12790.

[42] Kitsu Iglesias, L.; Antonio, E. N.; Martinez, T. D.; Zhang, L.; Zhuo, Z.; Weigand, S. J.; Guo, J.; Toney, M. F. Revealing the Sodium Storage Mechanisms in Hard Carbon Pores. *Advanced Energy Materials* **2023**, *13*, 2302171.

[43] Wang, F.; Chen, L.; Wei, J.; Diao, C.; Li, F.; Du, C.; Bai, Z.; Zhang, Y.; Malyi, O. I.; Chen, X.; Tang, Y.; Bao, X. Pushing slope- to plateau-type behavior in hard carbon for sodium-ion batteries via local structure rearrangement. *Energy & Environmental Science* **2025**, *18*, 4312-4323.

[44] Yin, X.; Lu, Z.; Wang, J.; Feng, X.; Roy, S.; Liu, X.; Yang, Y.; Zhao, Y.; Zhang, J. Enabling Fast Na^+ Transfer Kinetics in the Whole-Voltage-Region of Hard-Carbon Anodes for Ultrahigh-Rate Sodium Storage. *Advanced Materials* **2022**, *34*, 2109282.

[45] Zheng, Z.; Hu, S.; Yin, W.; Peng, J.; Wang, R.; Jin, J.; He, B.; Gong, Y.; Wang, H.; Fan, H. J. CO_2-Etching Creates Abundant Closed Pores in Hard Carbon for High-Plateau-Capacity Sodium Storage. *Advanced Energy Materials* **2024**, *14*, 2303064.

[46] Zhang, X.; Yang, W.; You, D.; Zhu, Z.; Li, X. Unlocking Plant-Derived Potential: Regulating Microcrystalline Structure Design of High-performance Hard Carbon Anodes via Cellulose Molecules. *Advanced Science* **2026**, *13*, e74653.

Electronic Supplementary Material

Cross-linking engineering of starch molecular topology tailoring hard carbon microstructure and sodium storage kinetics

Yongling Men[1], Qingsang He[1], Jiyue Hou[1], Yiyong Zhang[1], Ziyi Zhu[1*], Yingjie Zhang[1,2*], and Xue Li[1*]

[1]National and Local Joint Engineering Research Center of Lithium-ion Batteries and Materials Preparation Technology, Key Laboratory of Advanced Battery Materials of Yunnan Province, School of Metallurgical and Energy Engineering, Kunming University of Science and Technology, Kunming 650500, China

[2]Southwest United Graduate School, Kunming 650092, China

Address correspondence to Ziyi Zhu, zyzhu23@kust.edu.cn; Yingjie Zhang, zyjkmust@126.con; Xue Li, Lixue@kust.edu.cn

Supporting information to https://doi.org/10.26599/NR.2026.94909067

1. Experimental section

1.1. Materials preparation

Amylose and amylopectin were extracted using the complexing agent separation method. 20 g of commercially available corn starch was dissolved in 0.5 mol L^{-1} NaOH solution. The mixture was heated in a water bath with sufficient stirring. Then, n-butanol was added to the above mentioned dispersion. After washing, the precipitate obtained was high-amylose starch, named S-AM. For the remaining supernatant, two-fold volume of ethanol was added. The precipitate was collected by centrifugation, washed several times, and high-amylopectin starch was obtained, named A-AM. The centrifugation speed was 8000 r min^{-1} throughout the process.

S-AM was mixed with $(NH_4)_2HPO_4$ at a mass ratio of 5:1 and ball-milled for 30 min to obtain S-BM. A-BM was prepared following the same procedure using A-AM as the starting material. Under an argon atmosphere, S-BM and A-BM were heated to 200 ℃ and held for 3 h to complete the crosslinking reaction, yielding S-BM-200 and A-BM-200, respectively.

S-BM-200 and A-BM-200 were carbonized under an argon atmosphere by heating to 1400 ℃ at a ramp rate of 5 ℃ min^{-1} and held for 2 h, producing amylose-derived hard carbon (S-HC) and amylopectin-derived hard carbon (A-HC).

1.2. Materials characterization

S-AM and A-AM (10 mg each) were subjected to iodine staining for color observation. The amylose and amylopectin contents of S-AM and A-AM were determined using the dual-wavelength colorimetric method on a UV-6000 ultraviolet-visible spectrophotometer, with sample weighing performed on a PX124ZH analytical balance (0.1 mg precision). Dimethyl sulfoxide was used as the solvent for swelling degree tests. The types of functional groups for the materials were analyzed using Fourier transform infrared spectroscopy (FTIR). A Mini Flex600 model X-ray diffractometer (XRD) was used to analyze the microstructure of the materials. The thermal behavior and char-forming characteristics of the materials were analyzed using a STA449F3 synchronous thermal analyzer. Molecular structure and valence states were analyzed using a Thermofisher Escalab 250 Xi+ model X-ray

photoelectron spectrometer (XPS). Elemental analysis was performed using LECO NH836 oxygen-nitrogen-hydrogen analyzer, Elementar Vario Micro cube, and Agilent ICP-OES 5110. The pyrolysis process was tracked using a Thermo Scientific Nicolet iS50 Fourier transform infrared spectrometer coupled with a TA TGA55 thermogravimetric analyzer (TG-FTIR). Raman spectra were obtained using a LabSpec model confocal Raman microscope at a wavelength of 532 nm and a wavenumber range of 1000-2000 cm^{-1}. The morphology of the samples was observed using a TESCAN GA3 scanning electron microscope (SEM) and a JEM2100 high-resolution transmission electron microscope (HRTEM). The CO_2 adsorption-desorption isotherms obtained using the Micromeritics 3Flex device at 273 K were used to obtain the specific surface area and pore structure information. The N_2 adsorption-desorption isotherms obtained using the Quadrasorb evoTM model fully automatic specific surface area and pore size analyzer at 77 K were processed using the Brunauer-Emmett-Teller (BET) method. The closed pore structure of the materials was measured using a Saxess mc2 model small-angle X-ray scattering (SAXS) instrument, with a scattering vector range of 0.0001 to 0.5 nm^{-1}.

L_a and L_c are calculated from Scherrer equation [1] (1):

$$La\&Lc = \frac{\kappa\lambda}{\beta \cos\theta} \qquad (1)$$

In this formula, κ is scherrer constant (κ is 0.9 for L_c and κ is 1.84 for L_a), λ is the radiation wavelength, β is the half-height width of the (002) peak, θ is the reflection angle of (002) or (100).

The closed pore volume of the different HCs can be calculated using equation [2] (2):

$$V_{Closed\ Pore} = \frac{1}{\rho_{ture}} - \frac{1}{2.26} \quad (2)$$

1.3. Electrochemical performance measurements

Mix the active materials, carboxymethyl cellulose and conductive carbon in a mass ratio of 8:1:1 in ultrapure water, then evenly coat the mixture onto copper foil.

After vacuum drying, cut the foil into circular electrode. Assemble the 2016-type half-cell in a glove box filled with an inert atmosphere, where the H_2O/O_2 content is below 0.01 ppm: Use sodium metal as the counter electrode, 1 M $NaPF_6$ dissolved in 100 vol.% diethylene glycol dimethyl ether (1 M $NaPF_6$/DEGDME) as the electrolyte, and glass fiber as the separator.

Galvanostatic charge-discharge tests were conducted in a CT3002A model Land Battery Testing System, with a voltage range of 0.01-2.5 V. Galvanostatic intermittent titration technique (GITT) tests were performed under conditions of a pulse current of 20 mA g^{-1} and a relaxation time of 1800 s. Cyclic voltammetry (CV) tests were performed using the Land-E-Tech Muti-Range Precision Battery Tester M340A_V5C100MT8 with a scan rate of 0.1 to 1.0 mV s^{-1}. Electrochemical impedance spectroscopy (EIS) measurements were performed on an Autolab electrochemical workstation, with a frequency range of 10^{-2} to 10^5 Hz and an amplitude of 10.0 mV.

The full cell was assembled using commercial $Na_4Fe_3(PO_4)_2P_2O_7$ (NFPP) as the cathode material. NFPP, polyvinylidene fluoride, and conductive carbon are dissolved in N-methylpyrrolidone (NMP) at a mass ratio of 8:1:1, uniformly coated on aluminum foil, vacuum dried. The mass loadings of the A-HC anode and the NFPP cathode are ~1.5 mg cm^{-2} and ~5 mg cm^{-2}, respectively. Electrolyte of 1.0 M $NaPF_6$/DEGDME, with Whatman glass fiber (GF/B) as the separator to prevent short circuits. The operating voltage range of the full cell is 1.5-3.5 V.

The assembly process for in-situ EIS and in-situ Raman testing is similar to that for half-cells. In-situ EIS testing is conducted during discharging at a current density of 0.1 C (1 C=280 mAh g^{-1}), in-situ Raman testing is conducted during charging/discharging at the same current density, with a scanning range of 1000-2000 cm^{-1}.

Figures:

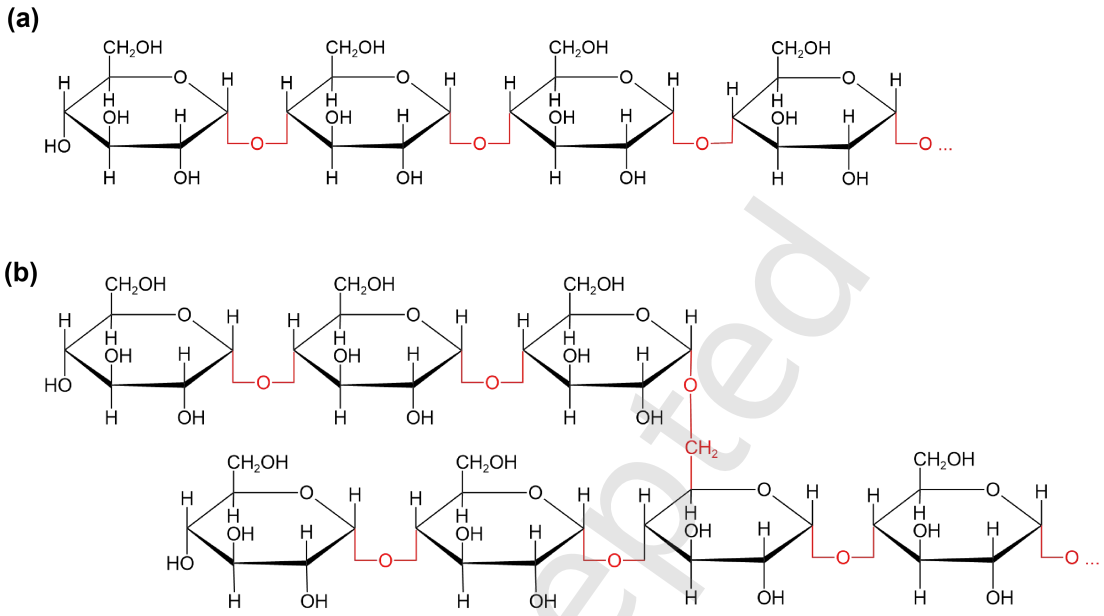

Figure S1. The molecular structure of (a) S-AM and (b) A-AM.

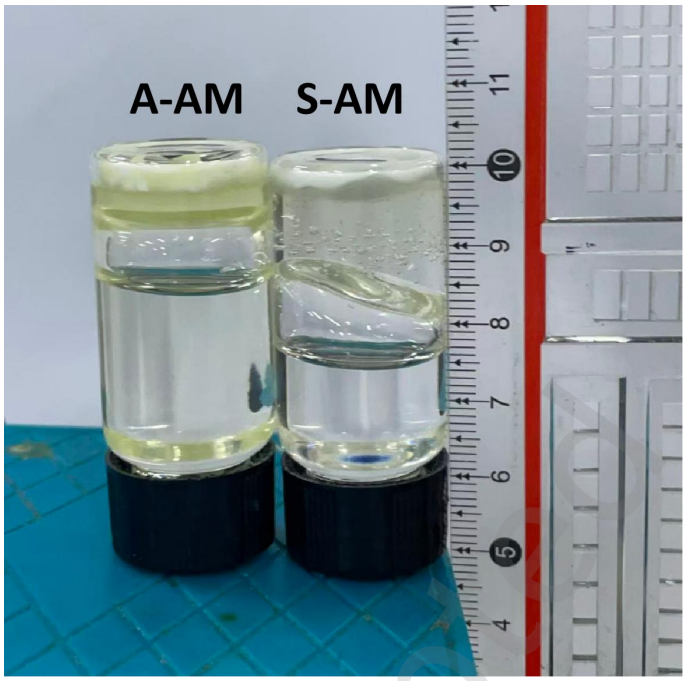

Figure S2. Results of the degree of swelling test.

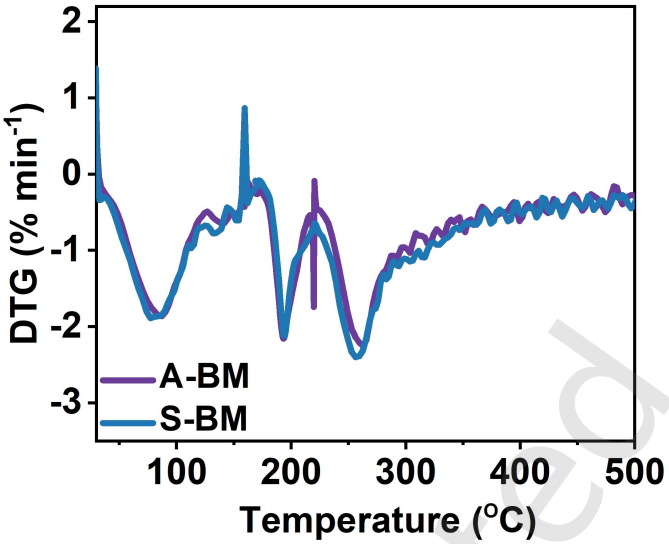

Figure S3. Differential Thermogravimetry curve.

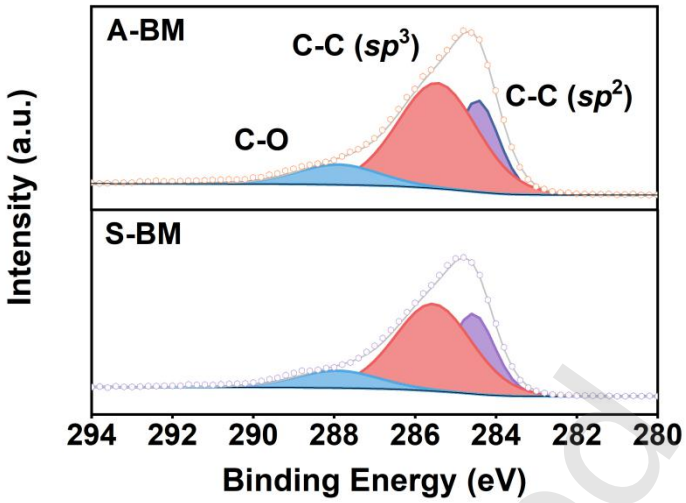

Figure S4. XPS spectra of C 1s of crosslinked samples.

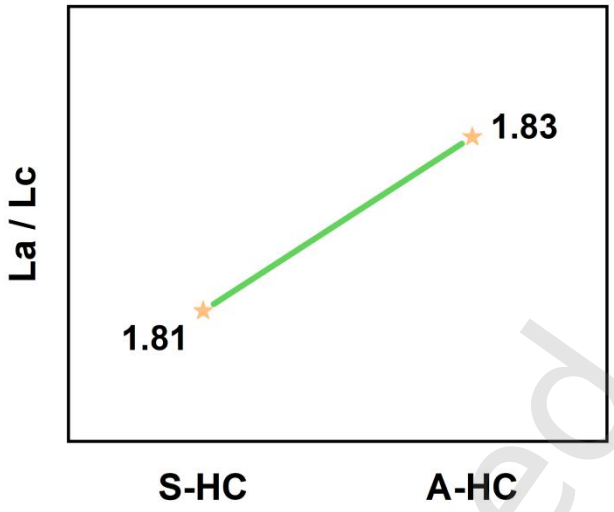

Figure S5. The degree of defects in hard carbons.

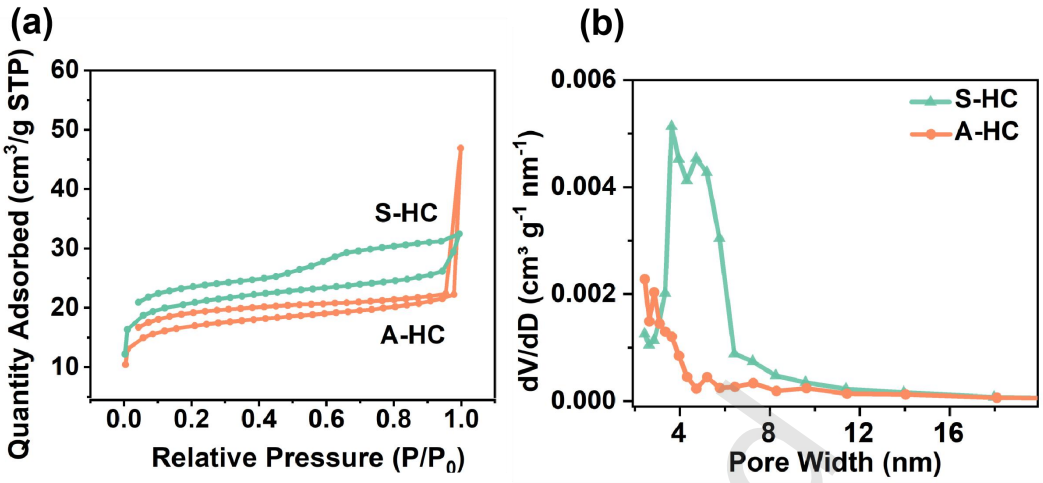

Figure S6. (a) N_2 adsorption-desorption isotherms and (b) pore size distribution curves of hard carbons.

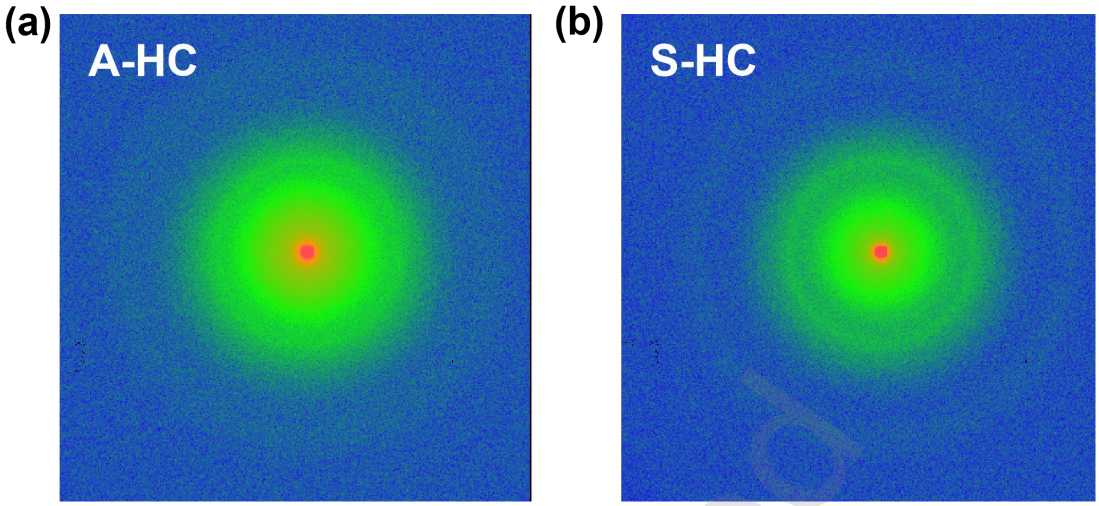

Figure S7. The 2D Small Angle X-ray Scattering (SAXS) pattern of hard carbons.

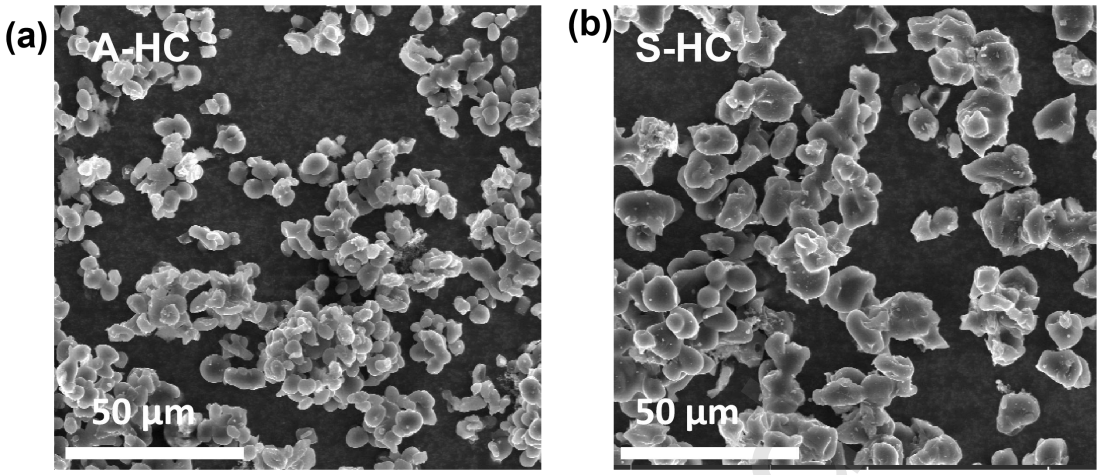

Figure S8. SEM images of (a) A-HC and (b) S-HC.

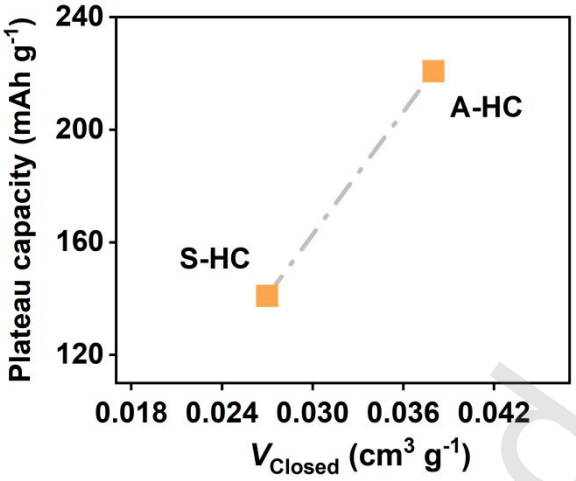

Figure S9. The correlation between closed-pore volume and plateau capacity.

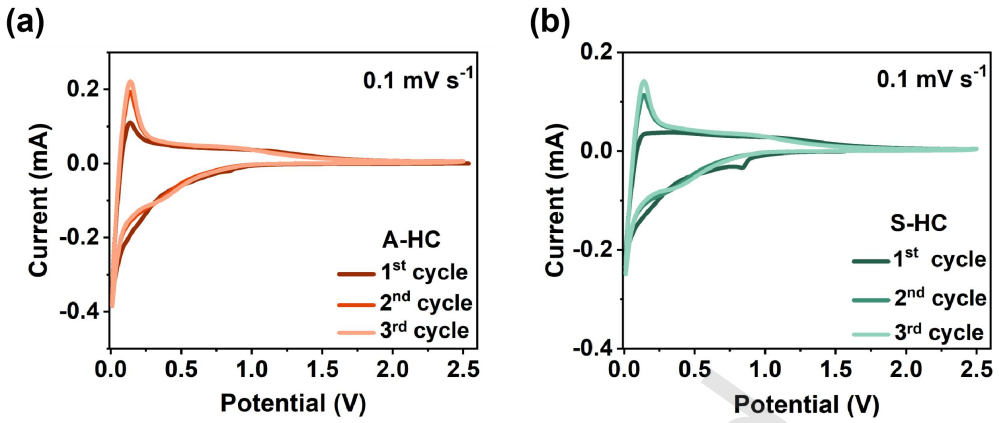

Figure S10. CV curves of the (a) A-HC and (a) S-HC electrodes.

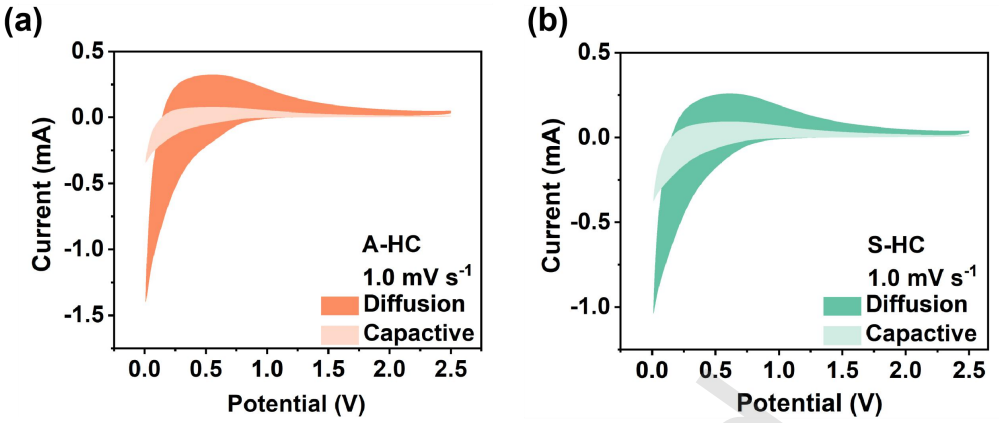

Figure S11. Capacitive and diffusive contribution at 1.0 mV s^{-1} scan rate of the (a) S-HC and (b) A-HC electrodes.

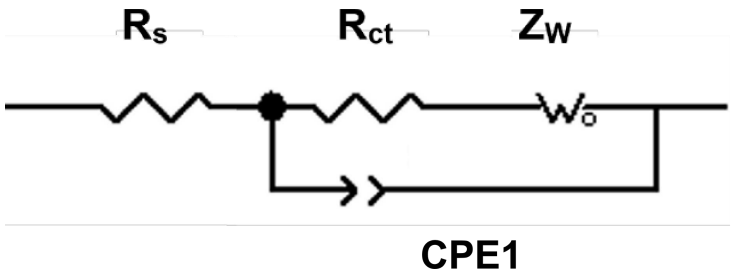

Figure S12. Equivalent circuit model.

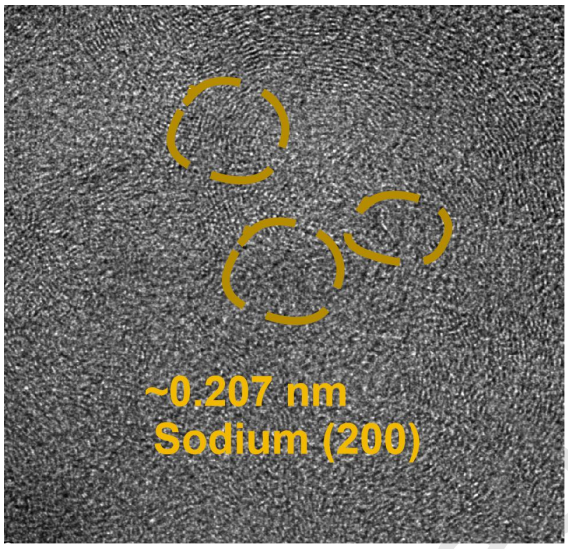

Figure S13. HRTEM images of the A-HC electrode after discharge to 0.01 V.

Tables:

Tables S1. Sodium storage performance of hard carbon materials at 0.1 C.

Sample	Amylose DW ($mg\ g^{-1}$)	Amylopectin DW ($mg\ g^{-1}$)	ratio
S-AM	787.86	328.74	2.40
A-AM	105.14	777.87	0.14

Table S2. Relative content of carbon species obtained by fitting the C 1s peaks of XPS spectra.

Sample	Element compositon from XPS (%)				
	C-C (sp^2) 284.57 (eV)	C-C (sp^3) 285.55 (eV)	C-O 287.92 (eV)	P/C	N/C
A-BM-200	32.15	39.54	16.94	0.069	0.059
S-BM-200	32.25	43.33	17.26	0.040	0.037

Table S3. Relative content of nitrogen and phosphorus species obtained by fitting the N 1s and P 2p peaks of XPS spectra.

Sample	Element compositon from XPS (%)					
	C-P-O_3 133.54 (eV)	C-O-P 133.94 (eV)	PO_4 134.60 (eV)	Amines 399.49 (eV)	N-5 400.17 (eV)	N-Q 401.80 (eV)
A-BM-200	1.29	1.33	3.51	1.304	1.036	2.9
S-BM-200	0.77	2.12	0.84	1.12	1.81	0.50

Tables S4. Elemental analysis.

Sample	N(%)	P(%)	C(%)
A-BM-200	3.25	5.56	48.50
S-BM-200	2.81	4.70	48.01
A-HC	1.03	0.077	-
S-HC	0.91	0.006	-

Tables S5. Structure parameters of the carbon materials.

Sample	*La* (nm)	*Lc* (nm)	*La*/*Lc*	d_{002} (nm)	I_D/I_G
A-HC	4.73	2.59	1.83	0.38-0.39	1.70
S-HC	3.59	1.98	1.81	> 0.4	1.81

Table S6. Pore structure parameters of HC.

Sample	S_{BET} (N_2) ($m^2\ g^{-1}$)	Vtotal (N_2) ($cm^3\ g^{-1}$)	True density ($g\ cm^{-3}$)	V_{Closed} ($cm^3\ g^{-1}$)
A-HC	63.08	0.0063	2.08	0.038
S-HC	78.19	0.0187	2.13	0.027

Table S7. Sodium storage performance of most recently reported biomass-derived hard carbon materials.

Precursor	ICE (%)	Performance (mAh g^{-1})	Ref.
Cellulose	75.6	365.8	[3]
Sepals of Palmyra palm fruit	-	320	[4]
Glucose	72.1	481.5	[5]
Loofah	76.5	317.5	[6]
Wood	93.5	309.7	[2]
Yeast	84.6	320.3	[7]
Walnut shell	90.1	374	[8]
Cotton cloth	-	239	[9]
Coconut shell	90.1	356	[10]
Cellulose and lignin	86.33	353.9	[11]
Coconut shell	67.95	311.1	[12]
Starch	88.51	346.01	**This work**

Table S8. The corresponding fitting parameters.

Sample	R_s (Ω)	R_{ct} (Ω)
A-HC	13.60	199.31
S-HC	10.46	289.92

References

[1] Wang, Y.; Yi, Z.; Xie, L.; Mao, Y.; Ji, W.; Liu, Z.; Wei, X.; Su, F.; Chen, C. Releasing Free Radicals in Precursor Triggers the Formation of Closed Pores in Hard Carbon for Sodium-Ion Batteries. *Advanced Materials* **2024**, *36*, 2401249.

[2] Zhang, X.; Yang, W.; You, D.; Zhu, Z.; Li, X. Unlocking Plant-Derived Potential: Regulating Microcrystalline Structure Design of High-performance Hard Carbon Anodes via Cellulose Molecules. *Advanced Science* **2026**, *13*, e74653.

[3] Zhao, B.; Li, X.; Shang, L.; Qiu, C.; Yuan, R.; Liu, H.; Liu, T.; Li, A.; Chen, X.; Song, H. Regulating oxygen functionalities of cellulose-derived hard carbon toward superior sodium storage. *Journal of Materials Chemistry A* **2024**, *12*, 5834-5845.

[4] Damodar, D.; Ghosh, S.; Usha Rani, M.; Martha, S. K.; Deshpande, A. S. Hard carbon derived from sepals of Palmyra palm fruit calyx as an anode for sodium-ion batteries. *Journal of Power Sources* **2019**, *438*, 227008.

[5] Qiu, C.; Li, A.; Qiu, D.; Wu, Y.; Jiang, Z.; Zhang, J.; Xiao, J.; Yuan, R.; Jiang, Z.; Liu, X.; Chen, X.; Song, H. One-Step Construction of Closed Pores Enabling High Plateau Capacity Hard Carbon Anodes for Sodium-Ion Batteries: Closed-Pore Formation and Energy Storage Mechanisms. *ACS Nano* **2024**, *18*, 11941-11954.

[6] Long, Q.; Zhang, F.; Qu, J.; Li, S.; Cheng, R.; Zhao, Y.; Guo, D.; Zhu, Z.; Zhang, H. Unraveling Synergistic Regulation Mechanism in Nitrogen/Sulfur Co-Doped Biomass-Derived Hard Carbon Toward Durable Sodium-Ion Battery Anodes. *ENERGY & ENVIRONMENTAL MATERIALS*, *n/a*, e70276.

[7] Feng, G.; Yang, X.; Liu, X.; Wang, Y.; Xie, Y.; Dong, P.; Jiao, X.; Xu, C.; Zhao, J.; Hu, Y.; Yang, W. Microbially glycolysis-regulated hard carbons for sodium-ion batteries. *Nano Energy* **2025**, *136*, 110728.

[8] Shi, W.; Wang, C.; Jian, Z.; Wu, F.; Liu, G.; Shen, X.; Huang, Y.; Cao, Y.; Zhang, F.; Li, X.; Liu, B.; Wang, Y.; Li, Y.; Wang, Z.; Cheng, H.; Lu, Z. Ethyl Acetate Vapor Induced Local Ordering in Hard Carbon for Stable Sodium-Ion Batteries. *Advanced Functional Materials* **2026**, *36*, e22214.

[9] Xu, Y.; Wang, Y.; Gu, Z.; Zhao, C.; Wu, X.; Silva, S. R. P.; Hou, B. Cellulose-grafting

boosted pyrolysis nucleation: Achieving low-temperature construction of hard carbon anodes with long low-voltage plateau and ultrafast Na storage kinetics. *Energy Storage Materials* **2025**, *75*, 104031.

[10] Zhong, Y.; Liang, W.; Lv, T.; Zhou, Z.; Zhou, H.; Yang, Z.; Ren, Z.; Zhao, H.; Wang, Y.; Hu, T.; Cui, M.; Feng, Z.; Meng, C. Facile One-Step Modification of Biomass Hard Carbon: Tailoring Hierarchical Microstructures for High-Energy-Density Sodium-Ion Battery Anode Materials. *Advanced Functional Materials* **2026**, *36*, e75776.

[11] Lin, P.; Wang, L.; Chen, J.; Fu, H.; Wang, X.; Zhong, Y.; Tu, J. Ultramicropore Engineering Bridges the Capacity-Kinetics Gap in Hard Carbon for Sodium-Ion Battery. *Advanced Energy Materials* **2026**, *16*, e70935.

[12] Wang, Y.; Cui, J.; Wang, M.; Shi, W.; Wang, L.; Yan, L.; Du, G.; Yang, Y.; Su, Q. Synergistic N/P Codoping Engineered Coconut Shell-Hard Carbon for High-Performance Sodium-Ion Battery Anodes. *Energy & Fuels* **2026**.